SF2A 2017
C. Reylé, P. Di Matteo, F. Herpin, É. Lagadec, A. Lançon, Z. Meliani, F. Royer (eds)

CLUMPY WIND ACCRETION IN SUPERGIANT X-RAY BINARIES

I. El Mellah[1], J.O. Sundqvist[2] and R. Keppens[1]

Abstract. Supergiant X-ray binaries (SgXB) contain a neutron star (NS) orbiting a Supergiant O/B star. The fraction of the dense and fast line-driven wind from the stellar companion which is accreted by the NS is responsible for most of the X-ray emission from those system. Classic SgXB display photometric variability of their hard X-ray emission, typically from a few 10^{35} to a few 10^{37}erg·s^{-1}. Inhomogeneities (a.k.a. clumps) in the wind from the star are expected to play a role in this time variability. We run 3D hydrodynamical (HD) finite volume simulations to follow the accretion of the inhomogeneous stellar wind by the NS over almost 3 orders of magnitude. To model the unperturbed wind far upstream the NS, we use recent simulations which managed to resolve its micro-structure. We observe the formation of a Bondi-Hoyle-Lyttleton (BHL) like bow shock around the accretor and follow the clumps as they cross it, down to the NS magnetosphere. Compared to previous estimations discarding the HD effects, we measure lower time variability due to both the damping effect of the shock and the necessity to evacuate angular momentum to enable accretion. We also compute the associated time-variable column density and compare it to recent observations in Vela X-1.

Keywords: X-ray binaries - wind accretion - massive stars - computational Astrophysics - Vela X-1

1 Introduction

The donor star in SgXB is a massive O/B Supergiant. The wind-launching mechanism of those stars differs from the models for low mass stars : the resonant line absorption of ultra-violet photons by partly ionised metal ions provides net linear momentum to the outer layers of the star. As the flow accelerates, it keeps tapping previously untouched Doppler-shifted photons (Lucy & Solomon 1970; Castor et al. 1975). Due to the high resulting supersonic speed of the wind, the orbiting NS can only capture a fraction of the mass lost by the star, contrary to Roche lobe overflow configurations. The high stellar mass loss rates associated to line-driven winds partly compensates for this inefficient mass transfer and the X-ray luminosity produced by the accretion process onto the NS can reach up to a few 10^{37}erg·s^{-1} (Walter et al. 2015).

But the hard X-ray emission from classical SgXB is not constant. The discovery of Super Fast X-ray transients (Sguera et al. 2005; Negueruela et al. 2006), where the photometric fluctuations are even more dramatic, urged the community to investigate the possible origins of this time-variability. A key-source of variability may be found in the very wind which feeds accretion. Indeed, line-driven winds are prone to a strong instability (the line deshadowing instability, LDI Lucy & White 1980; Owocki & Rybicki 1984) which produces internal shocks in the wind. It gives birth to higher density regions called clumps whose serendipitous accretion by the NS could, in principle, give a flare in X-rays.

The dimensions and shapes of these clumps have been recently computed in 2D radiative-HD simulations by Sundqvist et al. (2017) in a pseudo-planar stripe between one and two stellar radii. We build up on those results to design a 3D representation of the wind where the micro-structure and the contrasts are preserved. The latter provides outer boundary conditions upstream for a 3D spherical grid centred on the accretor. As the clumps enter the simulation space, we solve the equations of HD to follow their evolution towards the NS. Thanks to a stretching of the grid, we can monitor the flow from the upper scale, where the wind is still unperturbed by the presence of the NS, down to the NS magnetosphere, one thousand times smaller. In-between these scales, the flow is beamed by the gravitational field of the NS and forms a detached bow shock.

[1] CmPA, KU Leuven, Celestijnenlaan 200B, B-3001 Leuven, Belgium
[2] Instituut voor Sterrenkunde, KU Leuven, Celestijnenlaan 200D, B-3001 Leuven, Belgium

The object of the present paper is to study the impact of a realistic inhomogeneous wind on the time-variability of the X-ray emission and the column density between the accretor and the observer. In Section 2, we detail the numerical setup we rely on to derive the results on the flow structure, the mass accretion rate and the column density described in Section 3.

2 Numerical setup

To determine the dimensions and absolute position of our simulation space in the wind, we consider 2 different configurations whose parameters are given in Table 1 : a close and a wide-configuration with a small and large orbital separation respectively. The accretion radius is the key quantity to estimate the outer radius of our 3D setup. It corresponds to the critical impact parameter below which, in the ballistic sketch drawn by Hoyle & Lyttleton (1939) and Bondi & Hoyle (1944), the planar homogeneous incoming flow is likely to be accreted (for a review of BHL accretion theory, see Edgar 2004). It defines an accretion cylinder passing by the accretor and of main axis the bulk motion of the flow at infinity, and is given by :

$$R_{acc} = 2GM/v_{\infty}^2 \tag{2.1}$$

where G is the gravitational constant, M the mass of the accretor (here the NS) and v_{∞} is the velocity of the flow before it is significantly altered by the gravitational field of the accretor (here, the speed acquired by the line-driven acceleration mechanism). Since the front shock is expected to settle at a distance from the NS given approximately by R_{acc}, we need to inject the unperturbed supersonic wind at a larger distance. We set the outer radius of the simulation space, at $8R_{acc}$. We also account for the X-ray ionising feedback from the accretor by inhibiting the line-driven acceleration within this simulation space. Indeed, for a realistic X-ray luminosity of $2 \cdot 10^{36}$erg·s^{-1} and a critical ionisation parameter of 500 (Manousakis & Walter 2015), the ionization front is approximately located at $8R_{acc}$ upstream from the accretor. Within this region, the metal ions are too ionised to sustain the line-driven acceleration (Hatchett & McCray 1977).

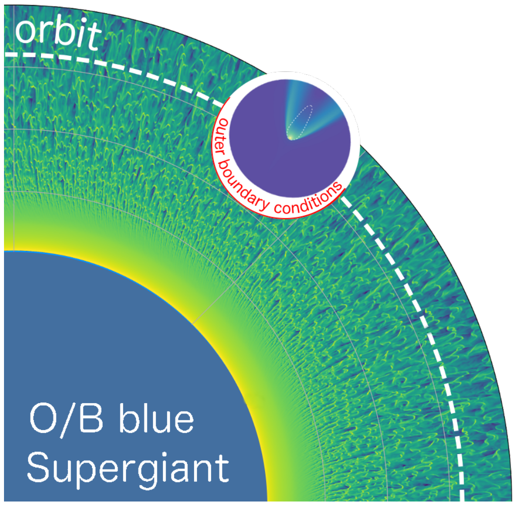

Fig. 1: Sketch of the stellar wind density map and of the position of the 3D simulation space centred on the compact object (CO), whose orbit around the Supergiant O/B star is shown. The insert in the upper right is the result of a 2D simulation of the accretion of a planar uniform flow from El Mellah & Casse (2015).

Table 1: Parameters of the two configurations considered

Parameters	Close config.	Wide config.
Stellar mass	$50M_\odot$	
Stellar radius R_*	$20R_\odot$	
Mass loss rate	$1.3{\cdot}10^{-6}M_\odot{\cdot}yr^{-1}$	
Orbital separation	$1.6R_*$	$2R_*$
NS mass	$1.3M_\odot$	$2M_\odot$
Effective velocity at NS	925 km·s^{-1}	1140 km·s^{-1}
Density at orb. sep.	$7.2{\cdot}10^{-15}$g·cm^{-3}	$3.6{\cdot}10^{-15}$g·cm^{-3}
Accretion radius	$\sim 4 \cdot 10^{10}$cm	

To inject the wind in the 3D simulation space, we first need to reconstruct a realistic 3D wind with the same stochastic properties. To do so, we transversely extend it (Figure 1) and compute the geometric average coefficient by coefficient of two 90-degrees rotated stripes. Once the histograms are corrected to retrieve the same distributions of values in all transverse directions, we sample this data on the surface of the spherical 3D grid embedded in the wind. It yields, as a function of time, the mass density, the speed and the pressure at the upstream outer boundary of the simulation space.

We work with a 3D spherical mesh centred on the accretor (Figure 2) and further detailed in Xia et al. (2017). To follow the flow in its journey to the NS and evaluate a representative mass accretion rate, we need to work with an inner boundary radius as small as possible. We set it to $R_{acc}/100$, deep within the shocked region. It also corresponds approximately to one thousand times the NS radius i.e. the outer rim of the NS magnetosphere ; within this region, a magnetohydrodynamical approach is required. We use a radially stretched

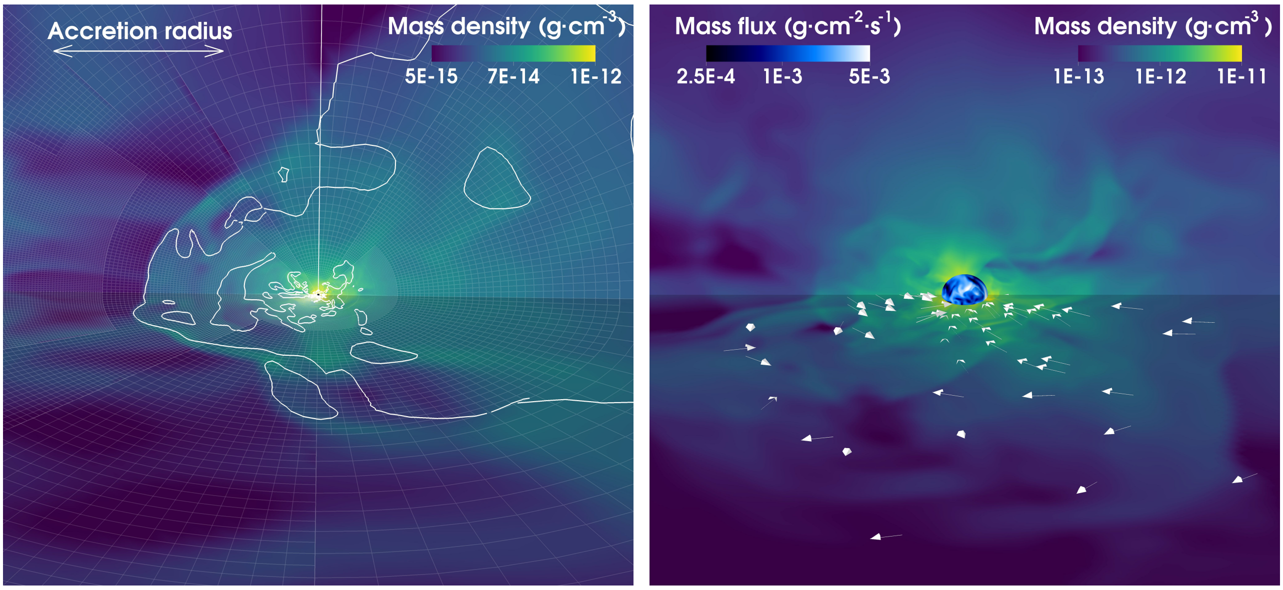

Fig. 2: Side view of a two-slice of a mass density colormap. The supersonic flow comes from the left and the polar axis is vertical. In the left panel, we zoomed in on the post-shock regions and the solid white line is the Mach-1 contour. In the right panel, we zoomed in even more and the vector field has been represented in the equatorial plane. The surface of the inner sphere, of radius $R_{acc}/100$, is colored with the local radial mass flux. See `http://homes.esat.kuleuven.be/~ileyk/clumps_HR.gif` for an animation of the inflowing clumps.

grid to span those almost 3 orders of magnitude at an affordable computational cost. Also, we enable Adaptive Mesh Refinement (AMR) in the outer regions upstream, in the aforementioned accretion cylinder, to resolve the clumps as they enter the simulation space. On the reverse, we inhibit AMR along the poles (set in the transverse plane).

3 Results

3.1 Structure of the flow

The flow adopts a structure qualitatively similar to the one obtained with a homogeneous inflow (El Mellah & Casse 2015). The wind with an impact parameter significantly larger than the accretion radius does not dissipate enough energy through the shock to be accreted and simply passes by the NS, flowing aways along the wake. On the reverse, the flow in the vicinity of the inflowing axis is shocked, dissipates its angular momentum in the turbulent shocked environment and flows through the inner border of the simulation space. The front shock goes back and forth, sometimes receding down to $R_{acc}/10$, but remains detached. No flip-flop instability is observed, in agreement with 3D simulations of BHL flows (Blondin & Raymer 2012).

3.2 Mass accretion rate

The mass accretion rate at the inner edge of the simulation space for the two configurations is plotted in Figure 3. The time-averaged values are in agreement with the order of magnitude given by the BHL approach (dashed black line in Figure 3) but it also displays an important time variability. Due to the presence of the shock, flares in mass accretion rate are not directly triggered by clumps. Sometimes, clumps with a large impact parameter pile up in the shock region before being flushed once matter with opposite angular momentum triggers dissipation. The shock tempers the influence of clumps, along with the need for clumps with a non-zero impact parameter to dissipate their angular momentum. The final time variability at the inner boundary of the simulation space is thus much smaller than what expected from accretion of purely ballistic clumps : the peak-to-peak variability we measure is of a factor of 10 in the close configuration, and 20 in the wide one. We interpret this trend of larger time variability at larger orbital separation as due to larger clumps as one moves away from the stellar surface.

An important qualitative conclusion to draw from the simulations is that an incoming large clump does

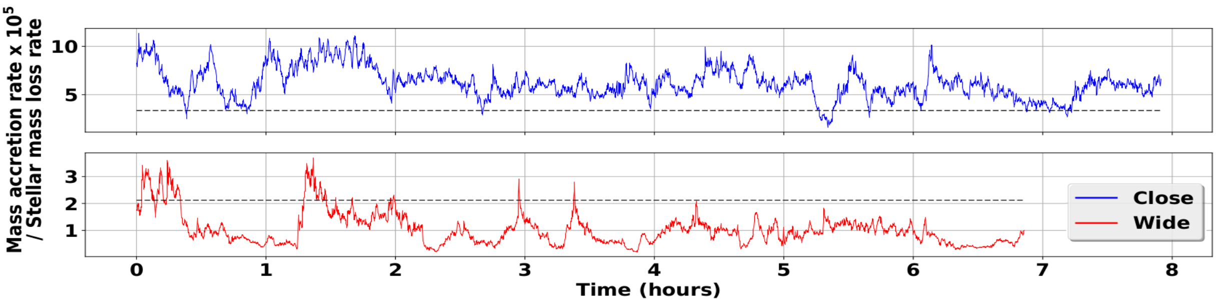

Fig. 3: Mass accretion rate at the inner boundary of the simulation space for the close ($a = 1.6\mathrm{R}_*$, third panel) and wide ($a = 2\mathrm{R}_*$, bottom panel) configurations. As a guideline, we plotted the BHL mass accretion rate for a smooth wind with the parameters from Table 1 (dashed black line).

not straightforwardly yield a flare in mass accretion rate. Conversely, it means that much caution should be taken when we try to trace back the origin of a flare to a clump mass. Between the ballistic clumps and the X-ray emission regions lie many different regions which dilute the clumps and trigger their own instabilities : time variability can be either enhance or damped depending on the physical conditions encountered by the flow as it gets accreted. If the time variability at the smaller scales is likely correlated to the one induced by the inhomogeneous wind, it is not directly related. Matter can pile up for quite long in intermediate regions (e.g. the shock or the corotation radius) before an instability which makes accretion possible is triggered.

3.3 *Column density*

Thanks to this numerical setup, we could also compute the column density between the NS and the observer as a function of time. Beyond the expected trend due to the orbital motion of the NS around its stellar companion, we measure a spread due to the random passing of unaccreted clumps along the line-of-sight, but also to the piling up of matter in the shocked region preceding flares. Results are given in Figure 4 for an edge-on inclination of the system and for the two configurations we considered. Grinberg et al. (2017) measured a column density varying between $0.72 \cdot 10^{22}\mathrm{cm}^{-2}$ to $5.76 \cdot 10^{22}\mathrm{cm}^{-2}$ between the orbital phases 0.21 and 0.25 (black rectangle in Figure 4. Both the close and wide configurations yield column densities lying within this range but they fail to explain this dramatic change in NH, which led Grinberg et al. (2017) to discard clumps happening to cross the line-of-sight as possible culprits. Indeed, leaving aside the uncertainty on the median value (which can be shifted by tuning, for instance, the stellar mass loss rate), the present model is unable to reach the maximal column density observed at those phases. It might be due to underlying structures within the magnetosphere that we could not study in detail with the present numerical setup. Notice however that given the orbital speeds at stake in this region, only isotropic structures could sustain such a high level of column density for so long. On the other hand, the minimal column density observed is preferentially achieved by the wide configuration, although marginally and at the end of the orbital phase interval.

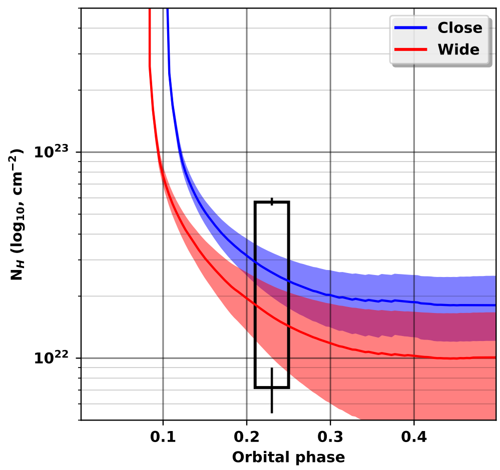

Fig. 4: Folded column density as a function of the orbital phase, for edge-on inclinations. The spread represents the 2-σ time-variability of N_H. The framed area shows the extent and the uncertainty on the variability observed by Grinberg et al. (2017), at orbital phases 0.21-0.25 (see text).

4 Conclusions

We ran 3D simulations of the accreted flow, centered on the accretor and with a mesh suitable to resolve the inhomogeneities in the upstream wind and follow them over almost 3 orders of magnitude in space. As the flow enters the sphere of influence of the NS, it is beamed toward it and forms a detached bow shock. The successive clumps cross this shock and, provided they loose enough energy and angular momentum, get accreted. As expected from the BHL approach of clump accretion (Ducci et al. 2009), the accretion proceeds mostly through the accretion cylinder. However, the present HD simulations show that the shock damps the time-variability with respect to the BHL estimation. Also, it introduces a time lag and a phase mixing since the shocked material associated to a clump is not straightforwardly accreted : it might be stored in a transient disc-like structure before accretion of matter with opposite net angular momentum triggers effective accretion.

Comparing to the X-ray luminosity diagrams at high energy, we showed that the wind micro-structure computed by (Sundqvist et al. 2017) and used in the present paper is not sufficient, per se, to retrieve the time-variability levels observed in classical SgXB such as Vela X-1 (Walter et al. 2015). The behavior at low luminosity matches the observations but the largest luminosity events require the possibility to quickly tap amounts of matter the clumps we considered here are not able to provide, even accounting for the intermediate shocked region where the flow can pile up. Other storage stages can appear once the NS magnetosphere and radiative cooling is accounted for (Illarionov & Sunyaev 1975; Bozzo et al. 2008; Shakura & Postnov 2017) or at the orbital scale (e.g. the X-ray ionizing feedback in Manousakis & Walter 2015). Also, the LDI simulations of Sundqvist et al. (2017) could yield larger clumps at a given orbital separation for a larger star or once clumping is enabled earlier on, near the stellar surface (where we know that clumps are already present, Cohen et al. 2011; Sundqvist & Owocki 2013; Torrejón et al. 2015). Given the comparative results for the wide and close configurations considered in this paper, the latter option would increase the time variability. It would also increase the time variability of the column density, bringing the results closer from what was observed by Grinberg et al. (2017) in Vela X-1.

IEM thanks the organizers of the High Energy Astrophysics session of the *Journées* of the French Astronomy Society for their interest in the present work. IEM has received funding from the Research Foundation Flanders (FWO) and the European Union's Horizon 2020 research and innovation programme under the Marie Skłodowska-Curie grant.

References

Blondin, J. M. & Raymer, E. 2012, Astrophys. J., 752, 30

Bondi, H. & Hoyle, F. 1944, Mon. Not. R. Astron. Soc., 104, 273

Bozzo, E., Falanga, M., & Stella, L. 2008, Astrophys. J., 683, 1031

Castor, J. I., Abbott, D. C., & Klein, R. I. 1975, Astrophys. J., 195, 157

Cohen, D. H., Gagné, M., Leutenegger, M. A., et al. 2011, Mon. Not. R. Astron. Soc., 415, 3354

Ducci, L., Sidoli, L., Mereghetti, S., Paizis, A., & Romano, P. 2009, Mon. Not. R. Astron. Soc., 398, 2152

Edgar, R. G. 2004, New Astron. Rev., 48, 843

El Mellah, I. & Casse, F. 2015, Mon. Not. R. Astron. Soc., 454, 2657

Grinberg, V., Hell, N., El Mellah, I., et al. 2017, submitted

Hatchett, S. & McCray, R. 1977, Astrophys. J., 211, 552

Hoyle, F. & Lyttleton, R. A. 1939, Math. Proc. Cambridge Philos. Soc., 35, 405

Illarionov, A. F. & Sunyaev, R. A. 1975, Astron. Astrophys., 39

Lucy, L. B. & Solomon, P. M. 1970, Astrophys. J., 159, 879

Lucy, L. B. & White, R. L. 1980, Astrophys. J., 241, 300

Manousakis, A. & Walter, R. 2015, Astron. Astrophys., 58, A58

Negueruela, I., Smith, D. M., Reig, P., Chaty, S., & Torrejón, J. M. 2006, Proc. X-ray Universe 2005 (ESA SP-604)

Owocki, S. P. & Rybicki, G. B. 1984, Astrophys. J., 284, 337

Sguera, V., Barlow, E. J., Bird, A. J., et al. 2005, Astron. Astrophys., 444, 221

Shakura, N. & Postnov, K. 2017, eprint arXiv:1702.03393

Sundqvist, J. O. & Owocki, S. P. 2013, Mon. Not. R. Astron. Soc., 428, 1837

Sundqvist, J. O., Owocki, S. P., & Puls, J. 2017

Torrejón, J. M., Schulz, N. S., Nowak, M. A., et al. 2015, Astrophys. J., 810, 102

Walter, R., Lutovinov, A. A., Bozzo, E., & Tsygankov, S. S. 2015, Astron. Astrophys. Rev., 23, 2

Xia, C., Teunissen, J., El Mellah, I., Chané, E., & Keppens, R. 2017, submitted